CaSn(OH)6 hydroxides, CaSnO3 oxides and CaSnF6 fluorides: synthesis and structural filiation. Cationic environment impact on Pr3+ doped compounds luminescence

Manuel Gaudon, Guillaume Salek, Malang Kande, Ines Andron, Christine Frayret, Etienne Durand, Nicolas Penin, Mathieu Duttine, Alain Wattiaux, Veronique Jubera

$CaSn(OH)_6$ hydroxides, $CaSnO_3$ oxides and $CaSnF_6$ fluorides: synthesis and structural filiation. Cationic environment impact on Pr^{3+} doped compounds luminescence

Manuel Gaudon [a], Guillaume Salek [a], Malang Kande [a], Ines Andron [a], Christine Frayret [b], Etienne Durand [a], Nicolas Penin [a], Mathieu Duttine [a], Alain Wattiaux [a], Véronique Jubera [a], ✉

[a] *Univ. Bordeaux, ICMCB, UMR 5026, F-33600 Pessac, France*
[b] *Laboratoire de Réactivité et Chimie des Solides (LRCS), UMR CNRS 7314, Université de Picardie Jules Verne (UPJV),Hub de l'Energie, rue Baudelocque, 80039 Amiens, France*

ARTICLE INFO

Keywords:
Stannate
Praseodymium
Crystal field
Luminescence
Nephelauxetic effect

ABSTRACT

$CaSn(OH)_6$, $CaSnO_3$ and $CaSnF_6$ compounds were elaborated from a "one-batch" synthesis route: the coprecipitation of the pure double hydroxide leads to pure double oxide or fluoride after annealing treatments under air or HF as anhydrous gas, respectively. Structural and morphological features of the three matrices were carefully investigated by X Ray Diffraction analysis and Scanning Electron Microscopy, respectively. In addition, the luminescent properties of the Pr-doped compounds were performed and compared. The nanometric size of the double hydroxide inhibits the luminescence. The interpretation of the emission spectra obtained for Pr-doped $CaSnO_3$ and $CaSnF_6$ compounds is based on the covalence/ionic balance of the M-O or M-F bonds.

1. Introduction

Because of their wide range of applications, perovskite-type alkaline earth metal stannates of formula $MSnO_3$ have been deeply investigated. Surprisingly, the luminescent properties of rare earth doped perovskite related structure are not largely reported yet [1-9]. However, promising results describe the photoluminescence of praseodymium doped perovskite as novel materials for multifunctional devices as the absorption lines of this rare earth overlaps the emission of commercial blue diode [10-19].

The $CaSn(OH)_6$, $CaSnO_3$ and $CaSnF_6$ exhibit obvious structural filiation. Indeed, these compounds have a structural network built on corner-sharing octahedra constituting the covalent skeleton. $CaSn(OH)_6$ and $CaSnF_6$ can be described as "double - ReO_3" structure in which Ca^{2+} and Sn^{4+} are strictly alternately distributed to form the octahedral chains. The octahedral sites of the double hydroxide are anisotropic, with low point group symmetry. Historically, $CaSn(OH)_6$ crystal was described as an orthorhombic perovskite structure with a *P n -3* space group, where the $Ca(OH)_6$ and $Sn(OH)_6$ octahedra share corners. More important, this framework can facilitate the mobility of the charge carriers, and then enhance the photocatalytic activity of $CaSn(OH)_6$ under light irradiation [20]. Nonetheless, the twist of the octahedral sites can also occur in such a way that a cubic unit-cell is maintained with *P n -3 m* space group [21], as for the Ca-Sn hydroxides (burtite) prepared in our work. The double fluoride is constituted of non-twisted isotropic octahedral sites that lead to a cubic unit-

✉ Corresponding autors.
E-mail address: veronique.jubera@u-bordeaux.fr; *Telephone number:* +33 5 4000 3703

Received: date; Accepted: date; Published: date

cell with *F m -3* m space group. Regarding $CaSnO_3$, the octahedral skeleton is built on [SnO_6] tilted octahedra (*P b n m* space group), the Ca^{2+} ions occupying the interstitial icosahedral sites. A scheme emphasizing the structural similarities and differences between the three studied compounds is reported (**Fig.1.**).

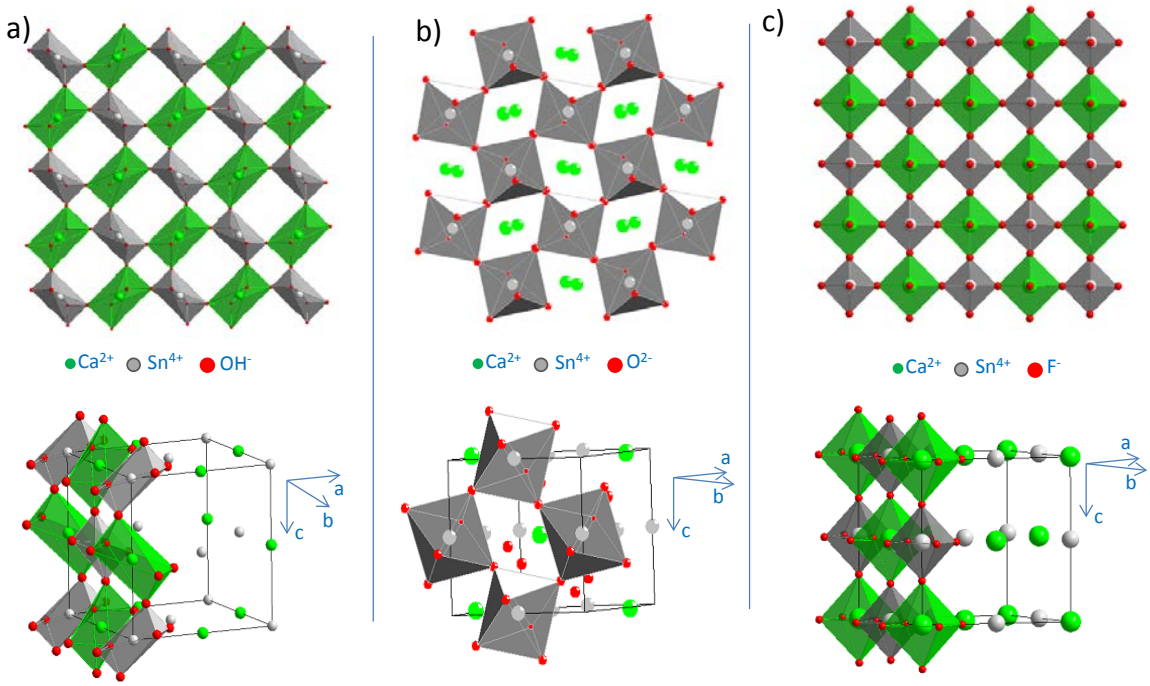

Fig. 1. a) Structural description of a) $CaSn(OH)_6$; b) $CaSnO_3$; c) $CaSnF_6$ crystals.

Even if a common skeleton is clearly visible and although cationic local environment is quite similar in the three matrices, the anionic group or ligands deeply change the nature of the chemical bonding. Because of their low phonon energy, their high transparency in the infrared and their stability under an exciting beam, fluoride hosts are of great interest for laser, up-converting or up-conversion materials [22-27]. Nevertheless, the increase of the chemical bonding ionicity is generally associated to an UV/blue shift of the spectral distribution, which can reduce drastically the efficiency of the absorption process regarding the matching with excitation sources.

Synthesis flow charts of $CaSn(OH)_6$ were recently described in literature [28-29]. $CaSnO_3$ perovskite compounds are typically synthetized at high temperature (over 1200°C) from traditional solid state reaction between CaO and SnO_2 oxide [30-32] Nevertheless, a two-step method was already employed for $CaSnO_3$ sample preparation including the synthesis at room temperature of the precursor $CaSn(OH)_6$ and then its conversion into $CaSnO_3$ by calcination [29,33-35]. $CaSnF_6$ compounds were typically made by solid state synthesis in a sealed tube [36]. By consequence, it represents a high challenge to find new synthesis routes of doped $CaSnF_6$ phases, cost-effective and with industrial feasibilities.

The first part describes the synthesis and the structural characterizations of the $CaSn(OH)_6$, $CaSnF_6$ and $CaSnO_3$ compounds. Especially, the description of a specific synthesis process based on the fluorination of $CaSn(OH)_6$ precursor is detailed. In a second part, the balance of the ionic-covalent bonds surrounding the luminescent ions is compared. We propose here to follow the evolution of the luminescent properties of Pr^{3+} doped compounds as a function of the chemical bonding nature. Crystal field effect will be highlighted through the *4f-4f* absorption and emission lines of trivalent praseodymium. These three compounds issued from a single synthesis batch and which present a strong structural filiation constitute school-case examples for studying the impact of the iono-covalence of the bonds around the luminescent ion, on the optical properties. This constitutes a first step to control and drive the emission properties to a targeted range.

2. Materials and Methods

2.1. Synthesis.

A co-precipitation process in aqueous solution allows obtaining the polycrystalline hydroxide compounds with $CaSn(OH)_6$ or Pr-doped $CaSn(OH)_6$ target formulae. $CaCl_2$ and $SnCl_4.5H_2O$ with eventually $Pr(NO_3)_3$, are firstly introduced into stoichiometric concentration into 25 mL of water. NaOH aqueous solution is added to the cationic solution in order to adjust the final pH to 10, 11.5 or 13. Once the precipitation has occurred, a maturation time of the precipitate under magnetic stirring is made during 2 hrs; the precipitate is filtered and washed with demineralized water. The solid residue is then crushed into an agate mortar. The as-prepared powders are then placed into a tubular furnace and treated at 1200°C – 12 hours under air, or between 100 and 250°C – 2 hours under HF gas atmosphere in order to obtain the mixed oxides and mixed fluorides, respectively. It can be noted that HF gas requires necessary warming: an inductive heater allows the heating avoiding HF and resistance contacts and the HF outgas is neutralized through KOH traps in order to be free of toxic exhaust gas production.

The $CaSnO_3$ and $CaSnF_6$ matrices and the corresponding 2 mol% Pr-doped oxide or fluoride ($CaSn_{0.98}Pr_{0.02}O_3$ and $CaSn_{0.98}Pr_{0.02}F_6$) are crushed before characterization.

2.2. X-ray diffraction analysis.

Powder X Ray Diffraction (XRD) patterns were collected on a Philips X'Pert MPD diffractometer operating in Bragg-Brentano geometry with a Cu $K_{\alpha 1,2}$ radiation ($10 < 2\theta < 130°$, step 0.02° and counting time of 30 s). Some of the diffraction patterns were refined using the full-pattern matching method (Le Bail) with the conventional reliability factors (Fullprof program package). Unit-cell parameters, zero-shift and peak profile parameters were refined.

2.3. ICP titration

ICP/OES (Inductively Coupled Plasma / Optical Emission Spectrometry) was conducted on Varian ICP/OES 720 ES apparatus.

2.4. SEM images

The Scanning Electron Microscopy (SEM) analyses were performed with a JEOL Field Emissive Gun - Scanning Electron Microscope (FEG-SEM) in order to characterize the crystallite (shape, size and special rearrangement) with a spatial resolution of about 1 nm.

2.5. Mossbauer investigation

^{119}Sn Mossbauer measurements were carried out using a constant-acceleration Halder-type spectrometer operating in transmission geometry with a room temperature ^{119m}Sn source (370 MBq, $CaSnO_3$ matrix). Thin absorbers containing about 10 $mg.cm^{-2}$ of Sn (^{119}Sn natural abundance 8.59 %) were placed into a liquid helium bath cryostat. In order to evaluate Sn^{4+} and/or Sn^{2+} local environments of the studied compounds, spectra were recorded from room temperature down to 4.2 K and the refinement of Mossbauer hyperfine parameters (δ isomer shift, Δ quadrupole splitting, Γ Lorentzian linewidth and relative areas) was performed using both homemade programs and the WinNormos® software (Wissenschaftliche Elektronik GmbH). The ^{119}Sn isomer shifts are referenced to $BaSnO_3$ at room temperature.

2.6. Photoluminescence analysis.

The photoluminescent properties were analyzed using a spectrofluorimeter Horiba Fluorolog3. Excitation spectra were corrected based on the variation of the incident flux. The emission spectra were corrected based on the transmission of the monochromator and the response of the

photomultiplier. The equipment used is composed of a 450 W xenon lamp, an excitation double monochromator, an emission double monochromator and a thermoelectrically cooled photomultiplier tube.

3. Results and discussion

3.1. Un-doped matrices

3.1.1. Synthesis and XRD characterization

The compound was obtained by the co-precipitation produced by the addition of NaOH into a Ca:Sn aqueous solution with 1:1 molar ratio and was analysed by XRD after drying and grinding steps (**Fig. 2.**).

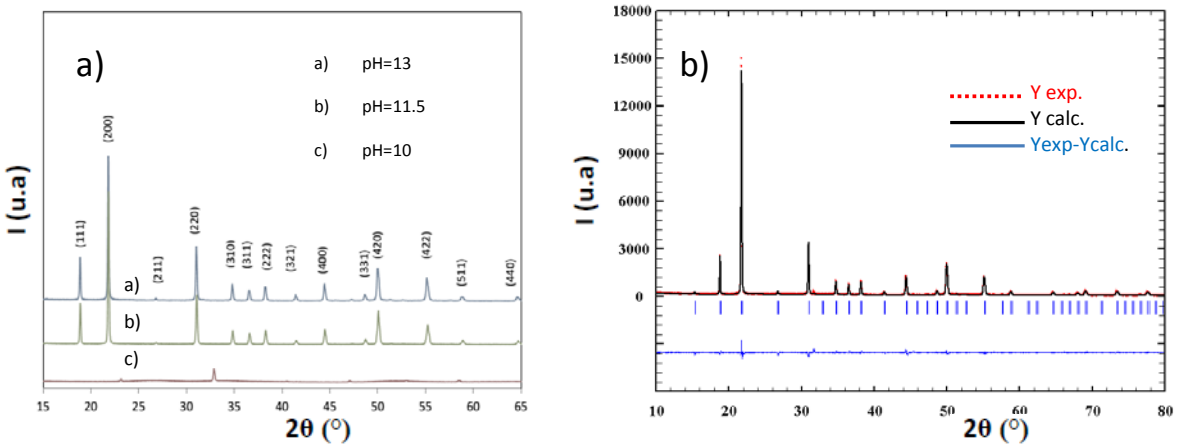

Fig. 2. (a) X-ray diffraction pattern of the $CaSn(OH)_6$ compound obtained by Ca-Sn coprecipitation at pH equal to 13, 11.5 and 10. (b) Full pattern matching analysis of $CaSn(OH)_6$ (pH= 11.5) diffractogram. Red and black lines are experimental and calculated spectra, respectively and the blue line represents the difference I(θ) = I exp - I cal.

The compound obtained by co-precipitation produced at pH =10 is different from the two other ones, obtained at pH=11.5 and 13. The first one is nearly amorphous. For the two latter, all the diffraction peaks can be clearly indexed as $CaSn(OH)_6$ compound with *P n -3 m* cubic space-group. A refinement of the unit-cell parameters was performed on the powder obtained at pH=11.5, using Fullprof method leading to unit-cell dimension: *a* = 8.1598(1) Å. The peak profile was refined using isotropic peak profile function (Caglioti function with *u, v, w* and shape as refined parameters). The quality of the refinement with a very flat difference signal (between the experimental and the calculated diffraction pattern) shows the presence of a pure phase constituted by isotropic crystals.

$CaSn(OH)_6$ double-hydroxide prepared by the co-precipitation at pH=11.5 was treated in air or HF atmosphere in order to obtain the $CaSnO_3$ perovskite and the double-fluoride, respectively.

The compound heat-treated at 1200°C under air is mainly $CaSnO_3$ phase. Traces of SnO_2 were observed (**Fig 3.a.**) Indeed, all the main peaks are indexed in the $CaSnO_3$ phase by considering an orthorhombic unit-cell with *P b n m* space-group. Unit-cell refinements lead to *a* = 5.6520(2) Å, *b* = 7.8825(3) Å and *c* = 5.5162(2) Å (**Fig. 3.b.**). SnO_2 traces constitute less than 2 weight% of the total mass. Interestingly, one can note that the SnO_2 traces tend to increase while the synthesis is performed from the double hydroxide obtained at pH = 13. Unfortunately, ICP titration is not enough accurate to be conclusive on a slight deviation of the Ca:Sn stoichiometric proportion. Anyway, the stoichiometric ratio between calcium and tin seems very sensible to the pH, without any impact of a slight stoichiometric deviation on the obtaining of a pure double hydroxide but with a drastic impact on the purity of the mixed $CaSnO_3$ oxide issued from air calcination of the double hydroxide.

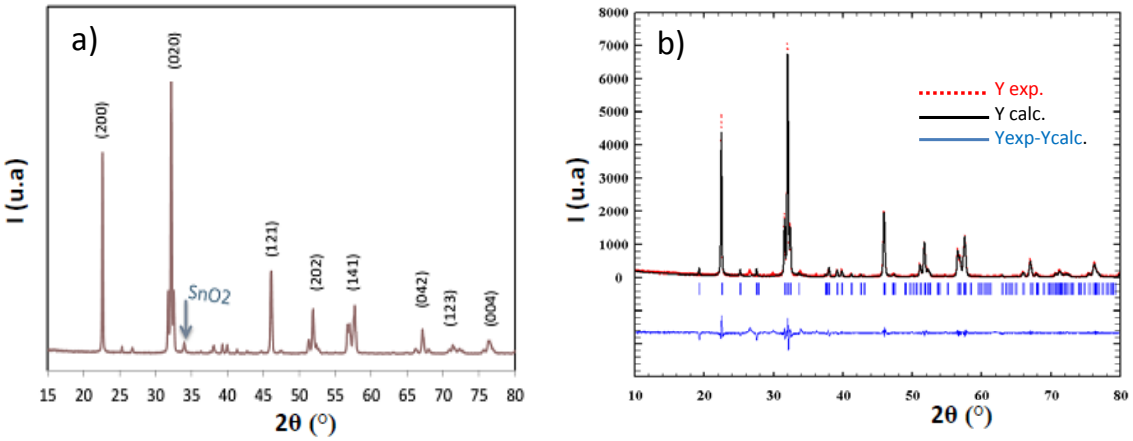

Fig. 3. (a) X-ray diffraction pattern of the $CaSnO_3$ compound obtained by annealing treatment at 1200°C under air of the $CaSn(OH)_6$ precursor. (b) Full pattern matching analysis of the corresponding compound diffractogram.

XRD patterns of the annealed hydroxide under HF gas atmosphere between 100°C and 250°C are illustrated in **Fig. 4.**, showing that: (i) below 150°C the $CaSnF_6$ phase is obtained but with many other impurities, (ii) after a heat-treatment at 200°C, a nearly pure $CaSnF_6$ phase is obtained, the diffraction peaks of the diffractogram being indexed as the *F m -3 m* cubic unit-cell. The refinement of the X-ray pattern allows the calculation of the *a* unit-cell parameter to *a* = 8.341(1) Å, what is in good agreement with literature. Nevertheless, traces of CaF_2 are still observed (non-indexed peak in **Fig. 4.b.**). HF treatments were also performed at higher temperatures. But a treatment above 250°C leads to the stabilization of undesired phases, *i.e.* a segregation occurs. Hence, the window for obtaining the $CaSnF_6$ phase is narrow.

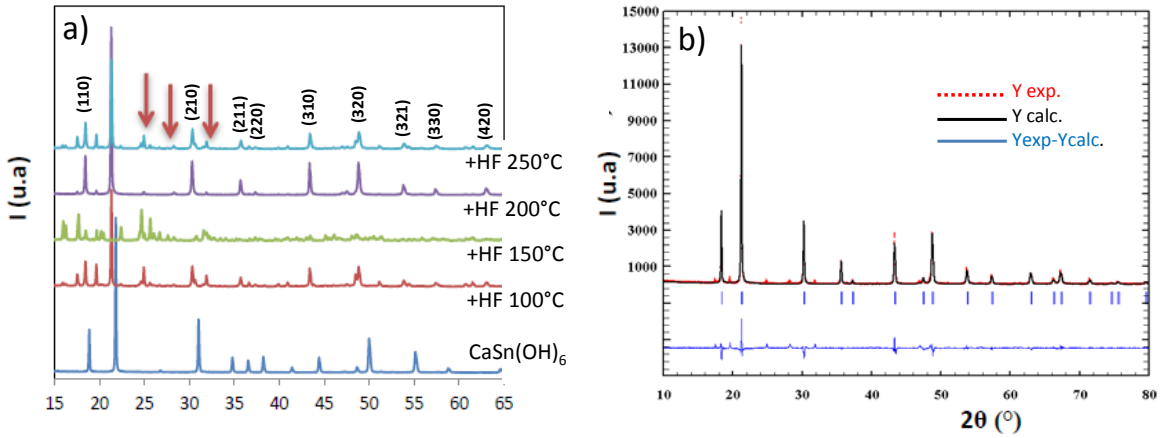

Fig. 4. (a) X-ray diffraction pattern of the $CaSnF_6$ compounds obtained by annealing treatment at 100, 150, 200, 250°C under HF atmosphere from the as-prepared $CaSn(OH)_6$ precursor. Red arrows indicate CaF_2 impurity. (b) Full pattern matching analysis of $CaSnF_6$ (HF 200°C) diffractogram.

3.1.2. SEM investigations on $CaSn(OH)_6$, $CaSnO_3$, $CaSnF_6$ matrices

The morphological investigations made using SEM technique allowed the comparison of the double-hydroxide, the perovskite oxide and the double-fluoride (**Fig. 5.**).

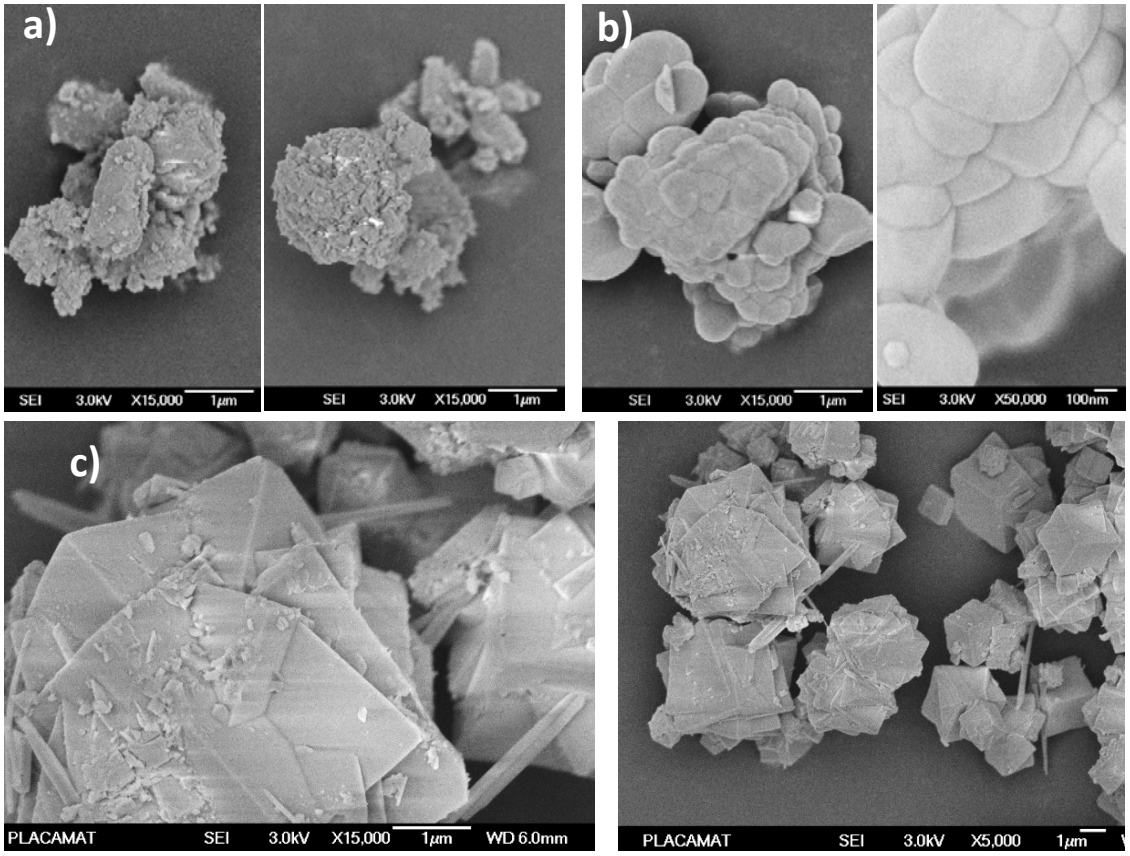

Fig. 5. SEM photographs of $CaSn(OH)_6$ (a), $CaSnO_3$ (b) and $CaSnF_6$ (c) compounds.

The raw double-hydroxide, obtained from a direct co-precipitation process, shows nanometric crystallite size, with isotropic agglomerates of about 1 micron diameter. The oxide obtained after high thermal treatment shows large crystallites (100 nm - 1 μm) with a quite large size distribution. The crystallites are strongly aggregated to form coherent grains of about 3-5 μm. Finally, the morphology of $CaSnF_6$ can be described as constituted by well-defined geometrical micrometric crystallites with intra-grown cubic polyhedra. It is quite surprising that the thermal treatment under HF at only 200°C can produce such an important crystallite growth. Some fine and long needles are also visible and have been characterized, as the CaF_2 impurities by EDX measurements which were previously observed on the X-ray diffraction patterns.

3.1.3. ^{119}Sn Mossbauer spectroscopy: $CaSn(OH)_6$, $CaSnO_3$, $CaSnF_6$ matrices

The three reference samples: $CaSnO_3$, $CaSn(OH)_6$ and $CaSnF_6$ were analyzed by ^{119}Sn Mossbauer spectroscopy at room temperature (**Fig. 6.**). The observed apparent singlets may be considered as paramagnetic quadrupole doublets with low quadrupole splitting (Δ) values (Table 1). For the three compounds, the calculated hyperfine parameters, isomer shift (δ) and quadrupole splitting, are characteristic of six-fold coordinated Sn^{4+} ions. The isomer shift is related to the charge density at the tin nucleus which is assumed to be a function of the number of 5*s* and 5*p* electrons (the contribution of *d* electrons is neglected). For tetravalent tin in octahedral site, the bonds may be considered as sp^3d^2 hybrid orbitals and the ratio of 5*s*/5*p* electrons is 1/3 [37]. Then, from the observed isomer shift values we can estimate the number of *s*-like electrons in the tin valence shell and the difference in electronegativity between tin and its ligands ($\Delta\chi$) by using the empirical relations proposed by Lees & Flinn [37] and Baggio & Sonnino [38], respectively. Thus, the differences observed in isomer shift values are consistent with a decrease of the *s*-electron density at the tin nucleus due to an increase of the ionic character of the Sn-X bond (n_s decreases) along with a higher electronegativity of X ($\Delta\chi$ increases).

Moreover, considering that the quadrupole splitting is mainly determined by distortions of the electronic charge around the Sn atom, slight variations in electric-field gradient and indirectly, in

crystal field intensity may occur between the mixed Ca-Sn oxide, hydroxide and fluoride. Indeed, the lower value of quadrupole splitting (and Lorentzian linewidth) was observed for the $CaSnF_6$ compound, indicating that the octahedral site and local environment of tin are more regular in the fluoride than in the hydroxide or oxide.

Finally, from low-temperature (4.2 K) measurements (Fig. SI-1), no Sn^{2+} signature was evidenced for the three analyzed samples.

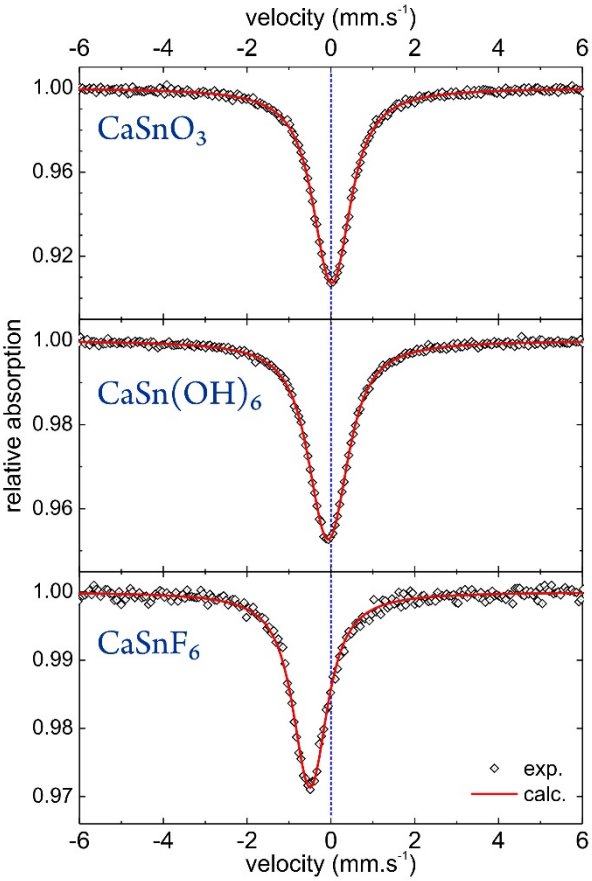

Fig. 6. Room temperature experimental (black dots) and calculated (red line) ^{119}Sn Mossbauer spectra of the $CaSnO_3$, $CaSn(OH)_6$ and $CaSnF_6$ compounds.

Table 1. ^{119}Sn Mossbauer hyperfine parameters determined from the fitted room temperature spectra of the Ca-Sn mixed oxide, hydroxide and fluoride. δ isomer shift (relative to $BaSnO_3$ at room temperature), Δ quadrupole splitting and Γ Lorentzian linewidth. n_s number of *s*-like electrons in the tin valence shell and $\Delta\chi$ the electronegativity difference between tin and its ligand, estimated from the isomer shift values [37-38].

T =293 K	δ (mm.s^{-1})	Δ (mm.s^{-1})	Γ (mm.s^{-1})	n_s	$\Delta\chi$
$CaSnO_3$	-0.001(2)	0.30(2)	0.91(1)	0.14	1.7
$CaSn(OH)_6$	-0.083(2)	0.32(2)	0.94(1)	0.11	1.8
$CaSnF_6$	-0.508(4)	0.22(4)	0.88(2)	0.00	2.2

3.2 Pr-doped $CaSn(OH)_6$, $CaSnO_3$ and $CaSnF_6$ samples

3.2.1. Synthesis and XRD Diffraction characterization

In a second step, Pr-doped $CaSn(OH)_6$, Pr-doped $CaSnO_3$ (from a 1200°C treatment under air) and Pr-doped $CaSnF_6$ (using a 200°C HF treatment) were investigated. X-ray diffraction patterns show a pure Pr-doped $CaSn(OH)_6$ hydroxide phase, a Pr-doped $CaSnO_3$ with traces of SnO_2 (same relative amount than for the non-doped matrix) and almost a pure Pr-doped $CaSnF_6$ compound along with a minor CaF_2 phase. The doping with Pr element does not seem to affect the results in comparison with the ones previously recorded for the non-doped matrices. Anyway, similar XRD patterns do not constitute a proof of the efficient incorporation of the doping ion within the crystalline structure. Indeed, all or part of the Pr^{3+} ions might remain in solution during the coprecipitation process and/or incorporated in a secondary phase which could be undetectable by XRD due to its too low content or to an amorphous state.

It can be noted that annealing treatment in air leads to the formation of a nearly pure Pr-doped perovskite (traces of SnO_2 being still detected with the same relative amount than for the matrix). Finally, a treatment at 200°C under HF leads to a Pr-doped $CaSnF_6$ fluoride phase.

3.2.1. Chemical analyses

The efficient introduction of 2 mol% of Praseodymium in substitution for Sn (i.e. corresponding to target composition: $CaSn_{0.98}Pr_{0.02}(OH)_6$) was investigated by ICP titration in order to check the Sn/Pr ratio in the hydroxide precipitate. The ICP results reported in **Table 2**, show clearly that the doping element are introduced with the adequate concentration into the precipitate. A blank measurement was made on the un-doped hydroxide for comparison. Without any doubt, from ICP measurement, the Pr^{3+} is in substitution of Sn^{4+} ion. It is well an aliovalent doping and the electroneutrality can be reached in such cases by anionic vacancies. Especially, ReO_3 and perovskite structural network are known, from the octahedral site with corner sharing as skeleton, to accept the occurrence of a quite large quantity of anionic vacancies. This could well explain the positioning of praseodymium in place of tin ions. We suppose that this Sn/Pr ratio remains unchanged in the oxide and fluoride stabilized by heat treatments of this initial powder.

Table 2. ICP titration results

Sample	Sn ($mg.L^{-1}$)	Pr ($mg.L^{-1}$)	Exp. Composition[1]
$CaSn(OH)_6$	123.7(1)	0	$CaSn(OH)_x$
$CaSn_{0.98}Pr_{0.02}(OH)_6$	110.3(1)	2.02(7)	$CaSn_{0.981}Pr_{0.019}(OH)_x$

[1] Experimental composition calculated considering 2 cations per unit-formulae.

3.2.3. Luminescence characterization

First of all, it has to be noted that all the three samples are white, *i.e.* they do not exhibit any absorption phenomenon in the visible range.

The luminescence of Pr^{3+}-doped $CaSn(OH)_6$ could not be detected even after heat-treatment processes in reducing conditions. Praseodymium might be stabilized at the 4+ oxidation state which would explain the total lack of radiative transition in this compound.

The luminescence of Pr^{3+} doped $CaSnO_3$ and $CaSnF_6$ is illustrated in **Fig. 7.** Because of the high thermal annealing under oxidizing atmosphere, praseodymium ions introduced in the SnO_2 impurity praseodymium ions must be stabilized at the tetravalent oxidation state. By consequence, they should not present visible luminescent properties. Concerning the trace of CaF_2 detected on the X-Ray diffraction patterns, we also eliminated the possibility of its contribution in the optical properties observed because the response of our sample clearly does not match with the luminescence of Pr^{3+} in the fluorite CaF_2 host lattice as a strong shift of the emission lines exists [39,40].

The absorption of the $CaSnO_3$ is detected below 300 nm as reported by Goto et al [6]. The emission curves are dominated by radiative de-excitation from the $^3P_0$ level. They consist in four main groups of lines corresponding to the intraconfigurational 4f-4f transitions *i.e*. $^3P_0 \rightarrow {}^3H_4$, $^3P_0 \rightarrow {}^3H_5$, $^3P_0 \rightarrow {}^3H_6$ and $^3P_0 \rightarrow {}^3F_2$ [41]. The corresponding energy levels are listed in Table 3. The energy level of $^3P_1$ and $^1D_2$ levels was determined using the semi-empirical method described by Antic-Fidancev [47] and based on the nephelauxetic scale (cloud expansion) of the rare earth ions. The Nephelauxetic effect reflects not only changes in the inter-electronic repulsion but also the spin-orbit interaction (depending on the number of *4f* electrons) of a central metal ion which impacts the position of the energetic levels. The nature of the ligand in the Pr^{3+} coordination polyhedron and its influence on the covalent bonding character notably impacts the energetic position and the intensity of emission lines. A clear red shift of the Pr^{3+}-$CaSnO_3$ is detected in comparison with the Pr^{3+}-$CaSnF_6$ lines reflecting the increased covalent character of the chemical bonding in the oxide (**Fig. 7.** and **Fig. SI-2.**). However, in none of the two emission curves, radiative transition has been observed from the $^1D_2$ as announced by Andrius Stanulis *et al.* [40] and Bingfu Lei *et al.* [48] respectively.

Table 3. Energy levels of the Pr^{3+} in several matrices

	Energy levels , Energy splitting of some transitions in cm^{-1} (in italic) And corresponding wavelengths range in nm (in parenthesis)							
System (coordination number of (Pr^{3+}) [ref]	**$^3P_2$**	**$^3P_1$ #**	**$^3P_0$**	**$^1D_2$ #**	**$^3F_2$/ $\Delta E_{(3P0 \rightarrow 3F2)}$ (Δλ range)**	**$^3H_6$/ $\Delta E_{(3P0 \rightarrow 3H6)}$ (Δλ range)**	**$^3H_5$/ $\Delta E_{(3P0 \rightarrow 3H5)}$ (Δλ range)**	**$^3H_4$/ $\Delta E_{(3P0 \rightarrow 3H4)}$ (Δλ range)**
$CaSnO_3$ (6) [this work]	21978 (455.5)	20967 (480.5)	20366 (491)	16700 (599)	5099/*57* (655-657.5)	4119/*755* (615.5-645.5)	1622/*855* (533.5-559)	0/*681* (491-508)
$CaSnO_3$ (6) [42]			20161 (496)			- (622.5)	- (530)	0/- (488)
Pb/Ge glass (-) [43]	22222	21141	20576	16835				- (486)
Sb oxide glass (-) [44]	22436 (445.7)	21173 (472.3)	20606 (485.3)	16849 (593.5)	- (652)	- (607)	-	-
$CaSnF_6$ (6) [this work]	22497 (444.5)	21385 (468.5)	20790 (481)	16943 (590)	5201 (641.5)	3898/*552* (592-612)	1633/*808* (522-545)	0/*445* (481-491.5)
LiF (6) [45]	22580 (443)	21351 (468)	20886 (479)	16990 (588)				
CsF (6) [45]	24210 (413)	-	20833 (480)	17089 (585)				
$LiLuF_4$ (8) [45]	22576 (443) 22727 (440)	21377 (468) 21452 (466)	20817 (478.3)	16835 17126 17384	4917/*447* (628-647)	4316/*73* (606-612)	2282/*151* (539-541)	0/*81* (480-482)

Energy position corresponding to the barycentre position deduced from Antic-Financev semi-empirical approach [47]

Taking into account the energetic position listed in Table 3, the $^1D_2 \rightarrow {}^3H_4$ transition is expected to peak at 600 nm in the oxide matrix but it is no detected here. Because of the low phonon energy of the fluoride matrix, non-radiative multiphonon depopulation of the $^3P_0$ level to the lower $^1D_2$ level is excluded in fluoride matrices. Thus no radiative desexcitation is neither expected from this level in

Pr^{3+}-$CaSnF_6$. The contribution observed at 590 nm is by consequence part of the $^3P_0$-$^3H_6$ groups of lines. But surprisingly, no emission from the $^3P_1$ level is observed as the $^3P_1 \rightarrow {}^3H_{5,6}$ should be detected at 520 nm and 598 nm respectively in Pr^{3+}-$CaSnO_3$ and at 506 nm and 572 nm respectively in Pr^{3+}-$CaSnF_6$.

The excitation curves are constituted by the $^3H_4 \rightarrow {}^3P_j$ ***4f-4f*** transitions. In addition a large band corresponding to the host lattice absorption is detected in the oxide matrix [6]. One cannot exclude a small contribution of a metal-metal charge transfer between Pr^{3+} and Sn^{4+} band as observed by Weiyi Jia *et al.* in Bi^{3+}, Pr^{3+} co-doped $CaTiO_3$ [49].

The effect of the crystal field on the ^3H_j level can be compared in both matrices (Table 3-*$\Delta(^3P_0 \rightarrow {}^{2S+1}L_J)$ value*). The highest values observed in the oxide can be correlated to the strongest octahedral tilting, which leads to significant changes in the local environment of the rare earth element substituting the A-site of the perovskite (Sn^{4+}). The distortion in the nonlinear Sn-O-Sn is expected to have a great influence of the 4f-4f transition probabilities, which is consistent with a higher emission intensity observed in the Pr^{3+} doped $CaSnO_3$.

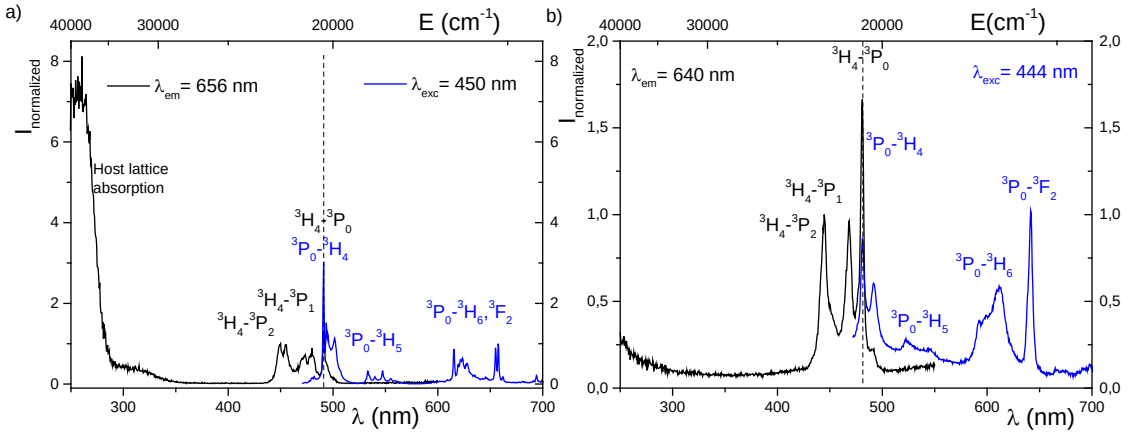

Fig. 7. Excitation and emission spectra of Pr-doped $CaSnO_3$ (a) and Pr-doped $CaSnF_6$ (b) samples.

As a consequence of the high sensitivity of the rare earth element to their cationic environment, the barycentre of the different Pr^{3+} energy levels is significantly lowered for the oxide compared to the fluoride matrices. The $^3P_0$ energy level of the studied matrices is reported in **Fig. 8.** among several other host lattices to clearly show the influence of the so-called nephelauxetic effect. It indicates that the octahedral environment of Pr^{3+} placed both matrices among those for which this effect is maximum.

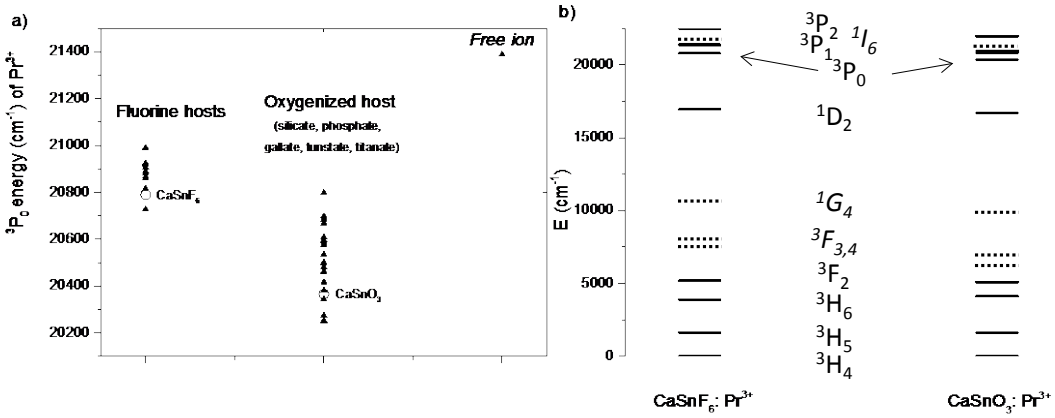

Fig. 8. Energy value of $^3P_0$ Pr^{3+} levels in several fluorine and oxygenized matrices. Each symbol is associated to data reported in the cited references [42-46; 50] (a) and energetic levels of Pr^{3+} in the oxide and fluoride studied compounds. Dotted lines are positioned for reading whereas full lines are deduced from experimental data (b).

The combination of a less-pronounced nephelauxetic effect and an increased ionic character of the chemical bonding in Pr^{3+} doped-$CaSnF_6$ results in a global blue shift of the emission color. The calculated trichromatic coordinates are equal to (0.46; 0.48) and (0.41; 0.42) for the oxide and for the fluoride compounds, respectively (**Fig. 9.**). The two samples exhibit an orange emission, but with a saturation greater for the oxide than for the fluoride, this latter being not so far to possess white emitting properties. Superimposed emission spectra of $CaSnO_3$: Pr^{3+} and $CaSnF_6$: Pr^{3+} 2% are presented in supplementary information (**Fig. SI-2.**).

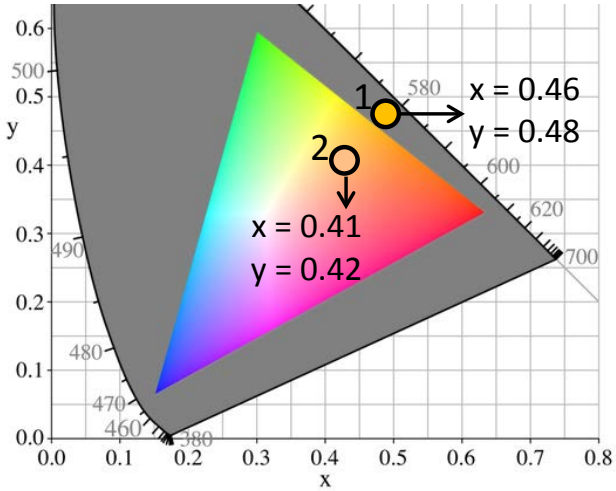

Fig. 9. Trichromatic diagram showing the positioning of Pr^{3+} emission in $CaSnO_3$ (1) and $CaSnF_6$ (2).

4. Conclusions

The synthetic route based on the calcination and/or fluorination of calcium hydroxystannate allow obtaining Pr^{3+}-doped $CaSnO_3$ and $CaSnF_6$ Pr^{3+} compounds. The change in metal-ligand bond covalence / ionicity (evidenced by ^{119}Sn Mössbauer spectroscopy) in the oxide, hydroxide, fluoride host matrices clearly influence the luminescence properties of the rare earth doped compounds.

Indeed, the high resolution of luminescence spectroscopy made possible to observe a significant shift and also a higher splitting of Pr^{3+} energy levels in the doped oxide host lattice in comparison with the fluoride one. Even if the coordination polyhedra of the rare earth element and their connection by common corner with other octahedra are similar in both host lattices, the nephelauxetic effect induces a noticeable reddening of the emitted color.

Supplementary Materials: The following are available online at www.mdpi.com/link, **Fig. SI-1.** and **SI-2.**

Acknowledgments: The authors thank the CNRS, the Nouvelle Aquitaine region. This study was carried out with financial support from the French State, managed by the French National Research Agency (ANR) in the frame of program PRIDE (n° ANR-16-CE08-0029). The author would like to associate Alexandre Fargues, ICMCB for his contribution in the technical aspect of luminescence spectroscopy (calibration and correction file validation).

Conflicts of Interest: "The authors declare no conflict of interest."

References

[1] Ueda, K.; Shimizu, Y.; Nagamizu, K.; Matsuo, M.; Honma, T. Luminescence and valence of Tb ions in alkaline earth stannates and zirconates examined by X-ray absorption fine structures. *Inorg. Chem.* **2017**, *56(20)*, 12625-12630

[2] Shi, M.; Zhao, H.; Zou, J.; Yang, B. B.; Li, Y.; Wang, Z.; Chang, C.; Li, W.. Preparation and characterization of a new long afterglow phosphor $CaSnO_3$: Yb^{3+}. *J. Mater. Sci.: Mater. Electron.* **2017**, *28(14)*, 10067-10072

[3] Vieira, Fagner T. G.; Casali, Graziela P.; De Lima, Severino J. G.; Siu-Li, Maximo; Longo, Elson; Maia, Ary Da Silva; De Souza, Antonio G.; Dos Santos, Ieda M. G. Photoluminescence in $SrSnO_3$:Fe^{3+} Perovskite. *Curr. Phys. Chem.* **2014**, *4(1)*, 21-29

[4] Kamimura, S.; Yamada, H.; Xu, C.-N. Strong reddish-orange light emission from stress-activated $Sr_{n+1}Sn_nO_{3n+1}$:Sm^{3+} (n = 1, 2, ∞) with perovskite-related structures. *Appl. Phys. Lett.* **2012**, *101(9)*, 091113/1-091113/4

[5] Nakamura, T.; Shima, M.; Yasukawa, M.; Ueda, K. Synthesis of Pr^{3+} doped or Tb^{3+}-Mg codoped $CaSnO_3$ perovskite phosphor by the polymerized complex method. *J. Sol-Gel Sci. Technol.* **2012**, *61(2)*, 362-366

[6] Goto, K.; Nakachi, Y.; Ueda, K. Photoluminescence properties of Pr doped and Tb-Mg codoped $CaSnO_3$ with perovskite structure *Thin Solid Films* **2008**, *516(17)*, 5885-5889

[7] Lu, Z.; Chen, L.; Tang, Y.; Li, Y. Preparation and luminescence properties of Eu^{3+}-doped $MSnO_3$ (M = Ca, Sr and Ba) Perovskite materials *J. Alloys Compd.* **2005**, *387(1-2),* L1-L4

[8] Endo, T.; Masuda, T.; Takizawa, H.; Shimada, M. Europium (2+) luminescence in $Sr_{n+1}Sn_nO_{3n+1}$ with layered perovskite structure *J. Mater. Sci. Lett.* **1992**, *11(19),* 1330-2

[9] Macke, A. J. H. Luminescence and energy transfer in the ordered perovskite system lanthanum magnesium tin titanium oxide ($La_2MgSn_{1-x}Ti_xO_6$) *Phys. Status Solidi A* **1977**, *39(1),* 117-23

[10] Shen, Y.; Qiu, K.; Zhang, W.; Zeng, Y.u. Red-emitting enhancement of $Bi_4Si_3O_{12}$:Sm^{3+} phosphor by Pr3+ co-doping for White LEDs application *Ceram. Int.* **2017**, *43(12),* 9158-9163

[11] Ma, S-Z.; Feng, W-L.; Chen, R.; Peng, Z-Q. $KSr_4(BO_3)_3$:Pr^{3+}: A new red-emitting phosphor for blue-pumped white light-emitting diodes *J. Alloys Compd.* **2017**, *700*, 49-53

[12] Tang, A.; Gu, L.; Zhang, H.; Zhao, Y.; Chen, H. Emission characteristics of Pr^{3+}-doped $InNbO_4$ used as a red-emitting phosphor for white LEDs *J. Optoelectron. Adv. Mater.* **2015**, *17(9-10),* 1243-1247

[13] Zhang, Y.; Huang, F.; Liu, L.; Liu, X.; Zheng, S.; Chen, D. Pr^{3+}/Ho^{3+} co-doped glass phosphors for application in warm white light-emitting diodes *Mater. Lett.* **2016**, *167*, 1-3

[14] Zhou, X.; Xiong, Z.; Xue, H.; Lin, Y.; Song, C. Hydrothermal synthesis and photoluminescent properties of $Li_2Sr_{0.996}SiO_4$:Pr^{3+}0.004 phosphors for white-LED lightings *J. Rare Earths* **2015**, *33(3),* 244-248

[15] Xiong, F. B.; Zhang, Z. W.; Lin, H. F.; Wang, L. J.; Xu, Y. C.; Zhu, W. Z. Luminescent properties of deep red light-emitting phosphors $NaGd(WO_4)_2:Pr^{3+}$ for blue LED *Opt. Mater. (Amsterdam, Neth.)* **2015**, *42*, 394-398

[16] Marin, R.; Sponchia, G.; Riello, P.; Sulcis, R.; Enrichi, F. Photoluminescence properties of YAG:Ce^{3+}, Pr^{3+} phosphors synthesized via the Pechini method for white LEDs *J. Nanopart. Res.* **2012**, *14(6),* 886, 13 pp

[17] Wang, L.; Zhang, X.; Hao, Z.; Luo, Y.; Wang, X-J.; Zhang, J. Enriching red emission of $Y_3Al_5O_{12}$: Ce^{3+} by codoping Pr^{3+} and Cr^{3+} for improving color rendering of white LEDs *Opt. Express* **2010**, *18(24),* 25177-25182

[18] Qi, X.; Liu, C-M.; Kuo, C-C. Pr^{3+} doped $LaTiNbO_6$ as a single phosphor for white *J. Alloys Compd.* **2010**, *492(1-2),* L61-L63

[19] Zhou, Y.; Liu, J.; Yang, X.; Yu, X.; Zhuang, J. A Promising Deep Red Phosphor AgLaMo2O8:Pr3+ with Blue Excitation for White LED Application *J. Electrochem. Soc.* **2010**, *157(3),* H278-H280

[20] Moshtaghi, S.; Salavati-Niasari, M.; Ghanbari, D. Characterization of $CaSn(OH)_6$ and $CaSnO_3$ Nanostructures Synthesized by a New Precursor. *JNC.* (*Journal of Nanostructures).* **2015,** *5,* 169-174

[21] Meng, S.; Li, D.; Sun, M.; Li, W.; Wang, J.; Chen, J.; Fu, X.; Xiao, G. Sonochemical synthesis, characterization and photocatalytic properties of a novel cube-shaped $CaSn(OH)_6$, *Catal. Commun.* **2011,** *12*, 972-975

[22] Biswas, K.; Balaji, S.; Ghosh, D.; Kalyandurg, A. Enhanced near-infrared to green upconversion from Er3+-doped oxyfluoride glass and glass ceramics containing $BaGdF_5$ nanocrystals *Int. J. Appl. Glass Sci.* **2017**, *8(2),* 204-215

[23] Kaminskii, A. A. Cascade stimulated emission from praseodymium(3+) and holmium(3+) ions in fluorine- and oxygen-containing crystals *Kvantovaya Elektronika (Moscow)* **1988**, *15(10),* 1943-4

[24] Yang, S.; Xia, H.; Zhang, J.; Jiang, Y.; Gu, X.; Zhang, J.; Wang, D.; Jiang, H.; Chen, B. Energy transfer and 1.8 μm emission in Tm3+/Yb3+ co-doped LiYF4 crystal *Journal of Nanoscience and Nanotechnology* **2016**, *16(1),* 537-541

[25] Yu, H.; Jiang, D.; Tang, F.; Su, L.; Luo, S.; Yan, X.; Xu, B.; Cai, Z.; Wang, J.; Ju, Q.; Enhanced photoluminescence and initial red laser operation in Pr:CaF2 crystal via co-doping Gd3+ ions *Mater. Lett.* **2017**, *206*, 140-142

[26] Soulard, R.; Doualan, J. L.; Braud, A.; Sahli, M.; Benayad, A.; Brasse, G.; Hideur, A.; Tyazhev, A.; Moncorge, R.; Camy, P. 1.87 μm laser operation by 980 nm pumping in Yb,Tm:CaF2 *Opt. Mater. (Amsterdam, Neth.)* **2017**, *72*, 578-582

[27] Petit, J.; Viana, B.; Goldner, P.; Roger, J-P.; Fournier, D. Thermomechanical properties of Yb3+ doped laser crystals: Experiments and modeling *J. Appl. Phys.* **2010**, *108(12),* 123108/1-123108/11

[28] Liu, T.; Ma, X.; Yang, L.; Li, H.; Lee, S.W.; Wang, Y. Highly enhanced photocatalytic activity of $CaSn(OH)_6$ through tuning $CaSn(OH)_6/SnO_2$ heterostructural interaction and optimizing Fe^{3+} doping concentration. *Appl. Catal. B-Environ.* **2017,** *217*, 256–264

[29] Wang, W.; Bi, J.; Wu, L.; Li, Z.; Fu, X. Hydrothermal synthesis and catalytic performances of a new photocatalyst $CaSnO_3$ with microcube morphology, *Scripta. Mater.* **2009,** *60*, 186–189

[30] Liu, Z., Liu, Y. Synthesis and luminescent properties of a new green afterglow phosphor $CaSnO_3$:Tb *Mater. Chem. Phys.* **2005,** *93(1)* 129-132

[31] Canimoglu, A.; Garcia-Guinea, J.; Karabulut, Y.; Ayvacikli, M.; Jorge, A.; Can, N. Catholuminescence properties of rare earth doped $CaSnO_3$ phosphor. *Appl. Radiat. Isotopes.* **2015**, *99*, 138-45

[32] Zhao, H., Shi, M., Zou, J., Yang, B., Li, Z. Wang, Z., Chang, C. Synthesis and luminescent properties of a new cyan afterglow phosphor $CaSnO_3$: Gd^{3+} *Ceram. Int.* ***2017,*** *43(2)* 2750-2755

[33] Lei, B., Li, B., Zhang, H., Li, W. Preparation and luminescence properties of $CaSnO_3:Sm^{3+}$ phosphor emitting in the reddish orange region *Opt. Mater. (Amsterdam, Neth.)* ***2007,*** *29(11),* 1491-1494

[34] Chen, X.Y.; Ma, C.; Bao, S.P.; Zhang, H.Y. Novel porous $CaSnO_3:Eu^{3+}$ and $Ca_2SnO_4:Eu^{3+}$ phosphors by co-precipitation synthesis and postannealing approach: A general route to alkaline-earth stannates *J. Alloys Compd.* **2010,** *497(1-2)* 354-359

[35] Cheng, H.; Lu, Z. Synthesis and gas-sensing properties of $CaSnO_3$ microcubes *Solid State Sci.* ***2008,*** *10(8),* 1042-1048

[36] Mayer, H.W.; Reinen, D.; Heger, G. Struktur und Bindung in Übergangsmetall-Fluoriden $MIIMeIVF_6$. Neutronenbeugungs-Strukturuntersuchungen an $CaSnF_6$, $FeZrF_6$, und $CrZrF_6$ *Journal of Solid State Chemistry* **1983**, *50(2)*, 213-224

[37] Lees, J.K.; Flinn, P.A. Mössbauer Effect in Tin Compounds : Interpretation of Isomer Shifts and Determination of the Nuclear Radius Change in ^{119}Sn. *J. Chem. Phys.* **1968**, *48(2),* 882-889.

[38] Baggio, E.M.; Sonnino, T. Isomer Shift and Electronegativity in Compounds of Tin and Group-VI Elements. *J. Chem. Phys.* **1970**, 52(7), 3786-3790.

[39] Hao Yu , Dapeng Jiang , Fei Tang , Liangbi Su , Saiyu Luo , Xigun Yan , Bin Xu , Zhiping Cai, Jingya Wang, Qiangwen Ju , Jun Xu, Enhanced photoluminescence and initial red laser operation in $Pr:CaF_2$ crystal via co-doping Gd^{3+} ions *Mater. Lett.* **2017,** *206,* 140–142.

[40] Boiaryntseva, I. A.; Gektin, A. V. The influence of praseodymium concentration on the luminescence properties of $Ca_{1-x}Pr_xF_{2+x}$ $(0.002 \le x \le 0.35)$, *Opt. Spectrosc.* **2012**, *113(2)*, 162-164

[41] Carnall, W. T.; Fields, P. R.; Rajnak, K. Electronic energy levels in the trivalent lanthanide aquo ions. I. Pr^{3+}, Nd^{3+}, Pm^{3+}, Sm^{3+}, Dy^{3+}, Ho^{3+}, Er^{3+}, and Tm^{3+} *J. Chem. Phys.* **1968**, *49(10)*, 4424-4442

[42] Stanulis A.; Katelnikovas A.; Van Bael M.; Hardy A.; Kareiva A.; Justel T. Photoluminescence of Pr^{3+}-doped calcium and strontium stannates *J. Lumin.* **2016**, *172,* 323–330

[43] Mohanty D. K.; Rai V. K. Photoluminescence studies of Pr3+ doped lead germanate glass *J Fluoresc.* **2011,** *21*, 1455–1460

[44] Som, T.; Karmakar, B. Pr_2O_3 doped KBS antimony oxide glass: Nephelauxetic effect of low phonon antimony oxide glass in absorption and photoluminescence of rare-earth ions *Spectrochim. Acta, Part A* **2011**, *79(5),* 1766– 1782

[45] Khokhryakov, A. A. ; Vershinin, A. O. ; Paivin, A. S. ; Lizin A. A. Electronic Spectra of Praseodymium Trifluoride Solutions in Molten Alkali Metal Fluorides *Russ. J. Inorg. Chem.* ***2015****, 60(12),* 1573–1577

[46] Cornacchia F.; Richter A.; heumann E.; Huber G.; Parisi D.; Tonelli M. Visible laser emission of solid state pumped $LiLuF_4:Pr^{3+}$ *Opt. Express*, **2007**, *15*, 992-1002

[47] Antic-Fidancev, E. Simple way to test the validity of $^{2S+1}L_J$ barycenters of rare earth ions (e.g. $4f^2$, $4f^3$ and $4f^6$ configurations) *J. Alloys Compd.* **2000**, *300-301,* 2-10

[48] Manu- Lei B.; Li B.; Zhang H.; Zhang L.; Cong Y.; Li W. Synthesis and luminescence properties of cube-structured $CaSnO_3/Re^{3+}$(RE=Pr,Tb) long-lasting Phosphors *J. Electrochem. Soc.* **2007**, *154(7)* H623-H630

[49] Jia W. ; Pérez-Andújar, A. ; Rivera, I. Energy transfer between Bi^{3+} and Pr^{3+} in doped $CaTiO_3$ *J. Electrochem. Soc.* **2003**, *150(7),* H161-H164

[50] Tanner, Peter A.; Yeung, Y.Y. Nephelauxetic effects in the electronic spectra of Pr^{3+} *J. Phys. Chem. A* **2013**, *117(41),* 10726-10735